

Journal of Materials Chemistry B

Materials for biology and medicine

rsc.li/materials-b



ISSN 2050-750X



Cite this: *J. Mater. Chem. B*, 2025, 13, 5521

Topology-dependent T_2 relaxivity in Fe_3O cluster-based MOFs for enhanced tumor monitoring via MRI[†]

Qiao Wang, Yimin Gong, Jianing Li, Dan Luo, Xin Zeng, Yun Ling, *
 Yaming Zhou  and Zhenxia Chen *

Metal–organic frameworks (MOFs) are crystalline porous materials with tunable structures, where metal ions or clusters serve as magnetic centers and organic ligands offer spatial separation. These characteristics, combined with their diverse topologies, make MOFs promising candidates for contrast agents (CAs) in magnetic resonance imaging (MRI). Herein we synthesized four MOFs based on the same triangular Fe_3O clusters with different topologies: MIL-101(Fe) (moo net), MIL-100(Fe) (mtn net), MIL-59(Fe) (pcu net), and MIL-88B(Fe) (acs net). To clarify the relationship between topologies and T_2 relaxivities, the MOFs were tailored into uniform, nanoscale spherical morphologies. Notably, the value of T_2 relaxivity for MIL-88B(Fe) with acs topology is nearly three times that for MIL-101(Fe) with moo topology at 7.0 T. By comparing the magnetic properties of Fe_3O molecular clusters and Ga-doped MIL-88B(Fe), our analysis demonstrated the significant advantage of MOFs with fixed arrays, adjustable components and diverse topologies in enhancing magnetic relaxation. Cellular MRI experiments further revealed that MIL-88B(Fe) could differentiate between M1 and M2 macrophages, highlighting its potential for monitoring tumor progression. These findings offer valuable insights into how MOF topology can be strategically utilized to enhance T_2 relaxivities for MRI applications.

Received 27th December 2024,
 Accepted 19th March 2025

DOI: 10.1039/d4tb02858a

rsc.li/materials-b

1. Introduction

Magnetic resonance imaging (MRI) has become an indispensable tool in clinical research fields due to its ability to non-invasively obtain high-resolution images of internal structures and functions.^{1–3} To enhance the contrast of images, particularly in deep tissue imaging, the use of contrast agents (CAs) is essential.⁴ Early CAs were primarily molecular-based, such as gadolinium⁵ and iron compounds.⁶ These agents work by altering the relaxation times of nearby water protons, thus improving the image quality. The magnetic resonance (MR) signals are largely influenced by several factors, including the molecular composition and the relaxation properties of the agent itself.⁷ The developments of nanotechnology have enabled the synthesis of nanoscale molecular assemblies, significantly improving the MRI performance by the aggregation effects from CAs.^{8,9} In addition to the aggregation effect, the size and morphology of CAs also play a crucial role in

determining the efficiency of CAs.¹⁰ For example, Cheon *et al.* discovered that the T_2 relaxivity of iron oxide nanoparticles (IONPs) shows a clear dependence on their sizes.¹¹ Similarly, Zhao *et al.* demonstrated that octapod-shaped IONPs exhibit a T_2 relaxivity 5.4 times higher than that of spherical IONPs of comparable volume.¹² Conceptualizing the magnetic center of a CA as a domain, the lattice structure and domain arrangement within a nanoparticle can significantly influence its MRI properties, making the regulation of domains a critical factor in optimizing CA performance. However, traditional dense structures based on rigid oxygen-bridges make precise control over internal magnetic domains unfeasible. These limitations emphasize the need for alternative materials to address the drawbacks of conventional IONPs in MRI research.

Metal–organic frameworks (MOFs) are crystalline porous materials constructed from organic linkers and metal ions/clusters, exhibiting well-defined structures and exceptional chemical tenability.^{13,14} MOFs offer a promising platform for the development of novel CAs with tailororable properties.^{15,16} Research studies on MOFs have demonstrated that relaxivity increases in a size-dependent manner.^{17,18} Khoobi *et al.* reported that the measured proton relaxation rates and contrast enhancement strongly depend on the size and aspect ratio of MIL-88B.¹⁹ The nano-sized metal clusters within MOFs serve

Shanghai Key Laboratory of Molecular Catalysis and Innovative Materials,
 Department of Chemistry, Fudan University, Shanghai, 200433, China.
 E-mail: yunling@fudan.edu.cn, zhxchen@fudan.edu.cn

† Electronic supplementary information (ESI) available. See DOI: <https://doi.org/10.1039/d4tb02858a>



as magnetic centers, while the organic ligands can modify the coordination environment and connectivity between metal centers, allowing for precise control over the relaxivity of CAs.²⁰ For example, Rathnayake *et al.* synthesized porous microstructures of isoreticular Fe-based MOFs (Fe-MOFs) and confirmed that the magnetic response is induced strictly by the localized electron density and spin density of states on Fe_3O domains.²¹ Although the diverse topologies of MOFs provide a unique opportunity to investigate how structural variation impacts MRI performance, a comprehensive understanding of the magnetism within MOFs for MRI research has not yet been fully explored. Given the unique architecture, MOFs represent an ideal platform to study and manipulate magnetic properties, meeting the essential structural criteria for advanced MRI applications.

In this work, we focus on the design and synthesis of MOFs featuring triangular Fe_3O clusters as magnetic lattices. These metal-oxo clusters, characterized by spin-canted magnetic interactions, are highly sensitive to structural changes, making them ideal candidates for studying topology-dependent effects on MR properties.^{22,23} Four Fe-MOFs with distinct topologies, MIL-101(Fe) (moo net), MIL-100(Fe) (mtn net), MIL-59(Fe) (pcu net), and MIL-88B(Fe) (acs net), were successfully synthesized.^{24–27} To minimize the influence of crystal face variations and magnetic anisotropy on T_2 relaxivities, we regulated the morphologies of four Fe-MOFs into isotropic spherical nanoparticles. From MIL-101(Fe) to MIL-88B(Fe), as the Fe_3O cluster density increased, we observed a gradual rise in both saturation magnetization and T_2 relaxivity. The value of T_2 relaxivity for MIL-88B(Fe) with acs topology is nearly three times that for MIL-101(Fe) with moo topology in 7.0 T. We further characterized the magnetic properties of Fe_3O molecular clusters and Ga-doped MIL-88B(Fe) for comparison. The results demonstrated the significant advantage of MOFs with fixed arrays, adjustable components and diverse topologies in enhancing magnetic relaxation. Finally, we demonstrated that MIL-88B(Fe) effectively distinguishes between M1 and M2 macrophages, highlighting its potential for monitoring tumor progression and showcasing its promise as a CA in MRI applications.

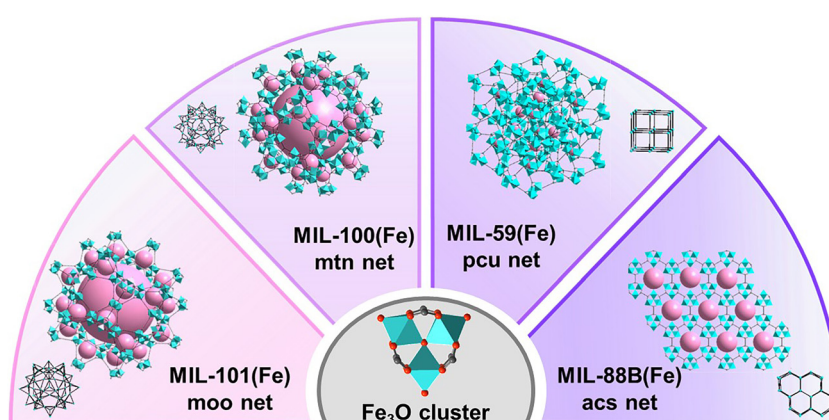
2. Results and discussion

2.1. Synthesis and characterization of four Fe-MOFs

Four Fe-MOFs were synthesized based on previously reported methods. Scheme 1 illustrates the distinct structures and topologies of these four Fe-MOFs constructed from the same Fe_3O cluster. As shown in Fig. 1a, the powder X-ray diffraction (PXRD) patterns matched well with the simulated patterns of MIL-101(Fe), MIL-100(Fe), MIL-59(Fe), and MIL-88B(Fe), confirming their high crystallinity and phase purity. Thermogravimetric curves of all four Fe-MOFs (Fig. S1, ESI[†]) exhibited three main weight loss stages: an initial 10% loss of around 100 °C, likely due to surface moisture; a second 40% loss between 100 and 500 °C, attributed to the decarboxylation of organic linkers, leading to framework collapse; and a final loss from 550 to 650 °C, marking complete framework decomposition. The nitrogen adsorption isotherms of MIL-101(Fe), MIL-100(Fe), MIL-59(Fe), and MIL-88B(Fe) are presented in Fig. 1b, with Brunauer–Emmett–Teller (BET) surface areas calculated as 2040, 1219, 300 and 37 $\text{m}^2 \text{ g}^{-1}$, respectively. These adsorption results are consistent with previous reports, showing that MIL-101(Fe) and MIL-100(Fe) exhibit well-defined large micro-pores, while MIL-59(Fe) and MIL-88B(Fe) exhibit dense, non-porous structures. Additionally, the FT-IR spectra of all four Fe-MOFs displayed a characteristic C=O stretching vibration peak in the range of 1600–1700 cm^{-1} , indicating the presence of carboxylate-containing organic ligands (Fig. S2, ESI[†]).

X-ray photoelectron spectroscopy (XPS) survey spectra, along with the corresponding binding energy spectra, of each element in four Fe-MOFs, are shown in Fig. 1c and d. These spectra provided further evidence for the successful synthesis of four Fe-MOFs, with iron existing in a trivalent oxidation state within the Fe_3O clusters. The XPS data clearly demonstrate the presence of Fe, C, and O, in agreement with the expected composition. These results confirm the successful incorporation of iron(III) into the MOF structure, along with high purity and structural integrity.

To eliminate the effects of crystal faces and magnetic anisotropy, we regulated all four Fe-MOFs into uniform



Scheme 1 Schematic illustration of the Fe_3O cluster and Fe-MOFs with different topologies.



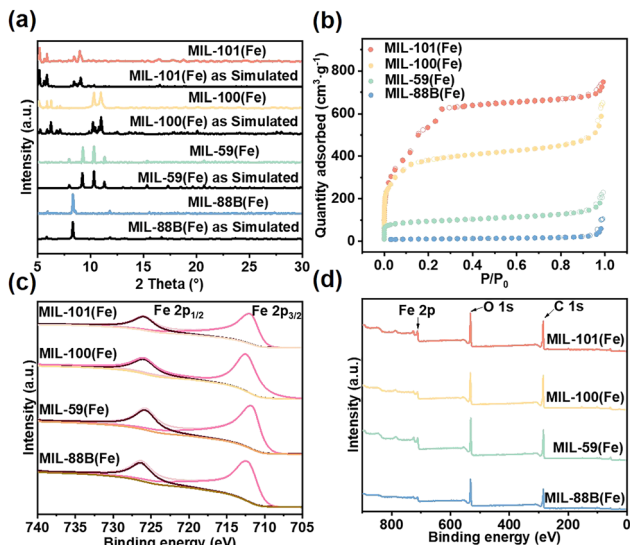


Fig. 1 (a) PXRD patterns, (b) N₂ adsorption–desorption isotherms at 77 K, (c) XPS spectra of Fe 2p levels, and (d) XPS spectra of MIL-101(Fe), MIL-100(Fe), MIL-59(Fe), and MIL-88B(Fe).

spherical nanoparticles of similar sizes. The morphology of four Fe-MOFs was thoroughly confirmed using scanning electron microscopy (SEM) and transmission electron microscopy (TEM). As shown in Fig. S3 (ESI[†]), the SEM images reveal that all four Fe-MOFs exhibited highly uniform particle sizes of approximately 150 nm, maintaining a well-defined spherical shape. TEM images also confirmed the spherical, uniform particle morphology, as shown in Fig. 2. TEM-EDS mapping displayed the homogeneous distribution of key elements, including Fe, C, and O, across the entire surface of the Fe-MOFs. This even dispersion suggests stable frameworks and further supports the successful formation of four Fe-MOFs with desired structural integrity. Collectively, all characterization techniques confirm the successful synthesis of four Fe-MOFs with distinct topologies, well-defined crystallinity and a uniform spherical morphology with consistent nanoparticle sizes.

2.2. T_2 relaxivities, T_2 -weighted imaging *in vitro*

The T_2 relaxivities of four Fe-MOFs with distinct topologies were measured under two different magnetic field strengths at

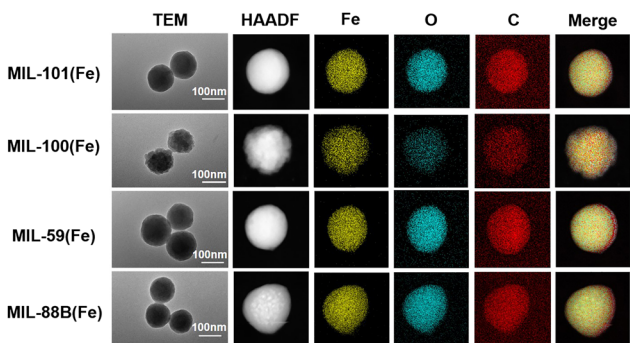


Fig. 2 TEM, HAADF-STEM, and EDX mapping images of MIL-101(Fe), MIL-100(Fe), MIL-59(Fe), and MIL-88B(Fe).

3.0 T and 7.0 T, respectively (Fig. 3a and b). Transverse relaxivity (r_2) was determined by fitting the relaxation rate as a function of concentration. At 3.0 T, the r_2 values of MIL-101(Fe), MIL-100(Fe), MIL-59(Fe), and MIL-88B(Fe) were calculated as 1.51 mL mg⁻¹ s⁻¹, 2.74 mL mg⁻¹ s⁻¹, 6.04 mL mg⁻¹ s⁻¹, and 8.76 mL mg⁻¹ s⁻¹, respectively. These values show that MIL-88B(Fe) with acs topology exhibits the highest T_2 relaxivity among the four Fe-MOFs at this field strength, suggesting a strong influence of topology on magnetic resonance properties. To further investigate the impact of magnetic field strength, measurements were repeated at 7.0 T. The r_2 values at this field were significantly increased to 16.43 mL mg⁻¹ s⁻¹ for MIL-101(Fe), 28.51 mL mg⁻¹ s⁻¹ for MIL-100(Fe), 35.03 mL mg⁻¹ s⁻¹ for MIL-59(Fe), and 40.28 mL mg⁻¹ s⁻¹ for MIL-88B(Fe), respectively. The markable r_2 value increases at 7.0 T indicating a pronounced sensitivity of T_2 relaxivity to magnetic field strength.⁷ Moreover, the consistent upward trend in r_2 values across the series, from MIL-101(Fe) to MIL-88B(Fe) at both 3.0 T and 7.0 T, highlights the critical role of MOF topology in influencing their relaxometric behavior under various magnetic fields.

As shown in Fig. 3c and d, the T_2 contrast effects of the four Fe-MOFs were also evaluated at both 3.0 T and 7.0 T, revealing a strong correlation between their topologies and MRI performance. Generally, Fe-MOFs with large pore sizes and surface areas, such as MIL-101(Fe) and MIL-100(Fe), exhibited relatively weak T_2 contrast effects. This may be attributed to the reduced efficiency of signal attenuation at low iron concentrations, suggesting that their porous structures limit sensitivity in T_2 -weighted imaging. In contrast, Fe-MOFs with small pore sizes and dense iron contents, such as MIL-59(Fe), demonstrate a significantly enhanced T_2 contrast effect, likely due to more efficient magnetic interactions. MIL-88B(Fe), with the densest iron content, displayed the strongest T_2 contrast effect among the four Fe-MOFs. Notably, even at a low concentration of

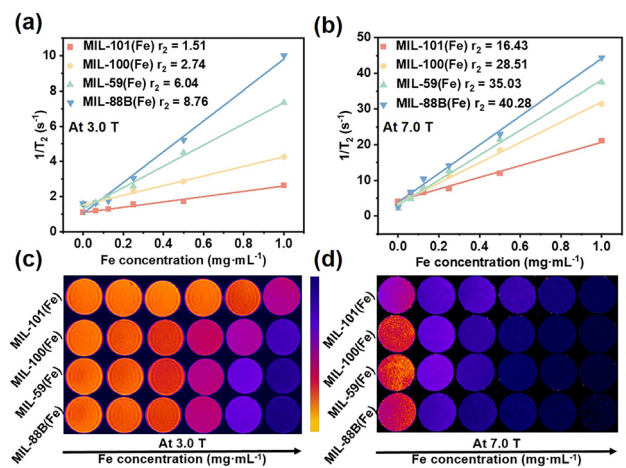


Fig. 3 T_2 relaxivities plot of MIL-101(Fe), MIL-100(Fe), MIL-59(Fe), and MIL-88B(Fe) at (a) a 3.0 T MR system and (b) a 7.0 T MR system. (c) T_2 -Weighted MR images of MIL-101(Fe), MIL-100(Fe), MIL-59(Fe), and MIL-88B(Fe) aqueous solution at (c) a 3.0 T MR system and (d) a 7.0 T MR system.

0.0625 mg mL⁻¹ at 7.0 T, MIL-88B(Fe) produced a distinctly dark signal, underscoring its potential for high-sensitivity MRI and precise diagnostic applications.

To further investigate the role of MOF framework in enhancing T_2 relaxivity, a discrete molecular Fe_3O cluster structure, $[\text{Fe}_3\text{O}(\text{O}_2\text{CPh})_6(\text{H}_2\text{O})_3]\text{ClO}_4$, which contains the same Fe_3O core as the Fe-MOFs, was synthesized and characterized (Fig. S4, ESI[†]). An *in vitro* MRI study revealed a r_2 value of only 9.48 mL mg⁻¹ s⁻¹ at 7.0 T, significantly lower than all four Fe-MOFs. This result suggests that the well-defined arrangement of Fe_3O clusters within the MOF framework does enhance the T_2 relaxivity, likely due to the structural effects of an extended network, which promote more effective magnetic relaxation.

Furthermore, the inherent spin frustration in Fe-MOFs can significantly limit their magnetic properties and reduce their effectiveness in magnetic resonance applications. To mitigate this issue, we selected MIL-88B(Fe) as a representative model and strategically substituted a portion of Fe^{3+} ions with non-magnetic Ga^{3+} ions. PXRD patterns as shown in Fig. 4a confirm that the crystalline structure and phase purity of MIL-88B remain intact across different Ga^{3+} doping levels. This substitution disrupts the spin-frustrated state by aligning the remaining two Fe^{3+} ions in an antiparallel configuration, thereby achieving a lower energy state. However, while this modification reduces spin frustration, it also partially cancels the material's magnetic properties due to the opposing spin orientations of the iron ions. Interestingly, when two Fe^{3+} ions are replaced by Ga^{3+} ions, leaving only one magnetic Fe^{3+} ion per cluster, the resulting structure exhibits the highest magnetic moment, as illustrated in Fig. 4b. This suggests that fine-tuning the doping ratio can optimize the magnetic properties by minimizing spin frustration while preserving or enhancing the overall magnetic moment. We then evaluated the T_2 relaxivities of MIL-88B(Fe), MIL-88B(Fe₂Ga), and MIL-88B(FeGa₂) at

7.0 T to assess the impact of Ga^{3+} doping on their magnetic resonance properties. As shown in Fig. 4c, the r_2 values increased progressively with higher gallium content, from 40.28 mL mg⁻¹ s⁻¹ for MIL-88B(Fe), 46.58 mL mg⁻¹ s⁻¹ for MIL-88B(Fe₂Ga) to 53.18 mL mg⁻¹ s⁻¹ for MIL-88B(FeGa₂). The T_2 -weighted MR images in Fig. 4d further support these findings. As the Ga^{3+} concentration increases, the signal intensity decreases, consistent with stronger T_2 contrast effects. Partial Ga^{3+} doping in Fe-MOFs suggests that the modified electronic environment around Fe^{3+} ions promotes more efficient magnetic relaxation, thus improving the material's performance as an MRI CA.

2.3. Magnetic properties

To further validate the magnetic properties of the four Fe-MOFs, magnetic hysteresis (M - H) measurements were conducted at 300 K (Fig. 5a), revealing their superparamagnetic behaviors. Notably, the saturation magnetization values exhibited a clear trend, increasing from 0.066 emu g⁻¹ in MIL-101(Fe) to 0.27 emu g⁻¹ in MIL-88B(Fe) (Fig. 5b). To better understand these magnetic properties, it is essential to analyze the electronic structures of four Fe-MOFs. The insulating behavior of Fe-MOFs arises from the limited overlap between the d-orbitals of the metal centers and the p_z orbitals of the organic ligands, which restricts electron delocalization. As a result, the electron density remains localized within the Fe_3O clusters, forming isolated magnetic domains within the MOF crystal structure.^{21,28} In the absence of an external magnetic field, thermal fluctuations cause random orientations of the Fe_3O clusters, yielding no net magnetism. However, under an applied magnetic field, the Fe_3O clusters align, producing a collective magnetic response. The topology of Fe-MOFs predominantly governs this alignment, thereby shaping their magnetic properties. With topologies that accommodate higher Fe_3O cluster densities, the magnetic moment increases, leading to a higher saturation magnetization. Herein, we defined the Fe_3O cluster density as the number of Fe_3O clusters per 1000 Å³, providing a quantitative foundation for subsequent calculations. As summarized in Table S2 (ESI[†]), the Fe_3O cluster densities for MIL-101(Fe), MIL-100(Fe), MIL-59(Fe), and MIL-88B(Fe) were calculated as 0.3989, 0.7098, 1.115, and 1.347 per 1000 Å³, respectively, reflecting a progressive increase

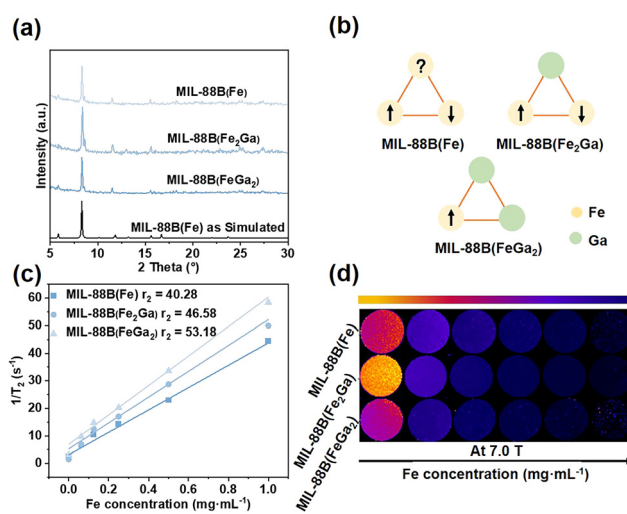


Fig. 4 (a) PXRD patterns of MIL-88B(Fe), MIL-88B(Fe₂Ga), and MIL-88B(FeGa₂). (b) Schematic illustration of MIL-88B with different metal doping ratios. (c) T_2 relaxivities plot, and (d) T_2 -weighted MR images of MIL-88B(Fe), MIL-88B(Fe₂Ga), and MIL-88B(FeGa₂).

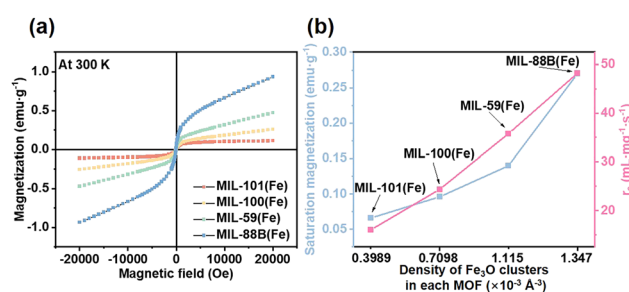


Fig. 5 (a) M - H loops of MIL-101(Fe), MIL-100(Fe), MIL-59(Fe), and MIL-88B(Fe) at 300 K. (b) T_2 relaxivities and saturation magnetization versus the density of Fe_3O clusters.



across four Fe-MOFs. In line with this observation, XPS analysis confirms that MIL-88B(Fe) has the highest concentration of Fe atoms (Table S3, ESI[†]), reinforcing the relationship between Fe_3O cluster density and magnetic properties. Fig. 5b shows the relationship between increasing Fe_3O cluster density and enhanced saturation magnetization values. This tendency is also consistent between the Fe_3O cluster density and T_2 relaxivity values.

According to the traditional quantum mechanical outer-sphere theory, materials with consistent spherical morphology and elevated saturation magnetization will exhibit higher T_2 relaxivity.^{29–31} The equation for relaxivity (r_2) is expressed as

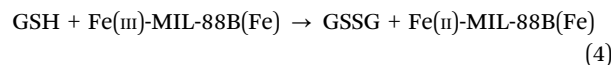
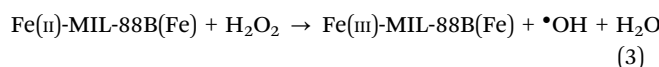
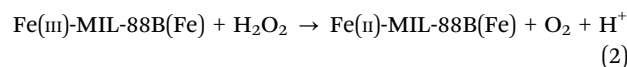
$$r_2 = (256\pi^2\gamma^2/405)\kappa M_s^2 r_2 / D(1 + L/r) \quad (1)$$

where M_s and r are saturation magnetization and effective radius of the magnetic nanostructure, respectively; D is the diffusivity of water molecules; L is the thickness of an impermeable surface coating, and κ is the conversion factor.³² This equation highlights how saturation magnetization (M_s) and Fe_3O cluster distribution directly impact T_2 relaxivity. The topology of MOFs, which specifically controls the distribution and density of Fe_3O clusters, plays a key role in optimizing both magnetic properties and relaxivity. MOFs with defined topology ensure an orderly and oriented distribution of clusters, which is essential for enhancing the vector sum of magnetic moments and, in turn, boosting the material's T_2 relaxivity, in line with the theoretical framework. In contrast, when molecular Fe_3O clusters are dispersed in a solvent, their spatial arrangement is disrupted, leading to a significant reduction in magnetic interactions and, consequently, lower T_2 relaxivity. Consequently, the fixed arrangement of Fe_3O clusters within MOFs, which can be further fine-tuned through topological control, provides a superior advantage in enhancing magnetic relaxivity.

2.4. Cellular MRI

In subsequent experiments, a model was developed to investigate the impact of different macrophage types on the MR properties of MIL-88B(Fe). M1 and M2 macrophages exhibit distinct biochemical profiles: M1 macrophages are typically in an inflammatory state with elevated hydrogen peroxide (H_2O_2) levels, while M2 macrophages are associated with anti-inflammatory responses, characterized by high glutathione (GSH) levels.³³ To simulate these conditions, MIL-88B(Fe) was exposed separately to H_2O_2 and GSH in solution. As illustrated in Fig. 6a and described by chemical eqn (2) and (3), MIL-88B(Fe) undergoes redox cycling between Fe(III) and Fe(II) when exposed to H_2O_2 , facilitated by the oxidizing environment. This process generates a stable negative contrast effect in T_2 -weighted MR images over time (Fig. 6b). Conversely, when MIL-88B(Fe) is exposed to GSH, the reductive environment gradually reduces Fe(III) to Fe(II), which possesses a lower magnetic moment and fewer unpaired electrons. This reduction progressively weakens the negative contrast effect, as described by eqn (4) and observed in the MR images. The reduction of Fe(III) to Fe(II) was further confirmed by XPS (Fig. 6c and Fig. S5, S6, ESI[†]). After treatment with H_2O_2 , the

Fe 2p spectra exhibited peaks at approximately 711 eV and 725 eV, corresponding to the Fe(III) $2p_{3/2}$ and Fe(III) $2p_{1/2}$ binding energies, respectively. A satellite peak characteristic of Fe(II) appeared at 715.9 eV, indicating that following the reaction with H_2O_2 , a portion of Fe(III) was reduced to Fe(II). For MIL-88B(Fe)-GSH, the binding energies of Fe $2p_{3/2}$ and Fe $2p_{1/2}$ shifted obviously to lower values following the reduction, with peaks at 709 eV and 722.4 eV corresponding to Fe(II). The satellite peak associated appeared at 715.1 eV, corresponding to the satellite peak of Fe(II). All Fe(III) nodes were reduced to Fe(II) due to the addition of an excess amount of GSH. These results provide direct evidence of the valence state change induced by GSH. Additionally, the M - H plot (Fig. 6d) demonstrated a significant decrease in saturation magnetization, further indicating that the magnetic properties of MIL-88B(Fe) were diminished after reduction by GSH.



Before proceeding with cellular MRI experiments, hyaluronic acid (HA) was conjugated onto MIL-88B(Fe) to enhance its biocompatibility. Zeta potential measurements in DI water confirmed successful HA conjugation, as the zeta potential shifted from +26.8 mV for MIL-88B(Fe) to -24.1 mV for MIL-88B(Fe)@HA (Fig. S7, ESI[†]). To further evaluate the colloidal stability of MIL-88B(Fe)@HA under biologically relevant conditions, dynamic light scattering (DLS) measurements were performed in different media. The hydrodynamic diameter was 220.2 nm in deionized water, whereas in physiological saline, it increased to 255.2 nm. This size increase can be attributed to the presence of Na^+ and Cl^- in saline, which compress the electrical double layer and weaken electrostatic repulsion between particles, leading to slight aggregation (Fig. S8, ESI[†]). To assess the cytotoxicity, MIL-88B(Fe)@HA was incubated with RAW264.7 macrophages, and cell viability was measured using the Cell Counting Kit-8 (CCK-8) assay. The cell viability results indicated that over 80% of cells remained viable at concentrations of up to 100 $\mu\text{g mL}^{-1}$ after 24 hours of incubation, suggesting that MIL-88B(Fe)@HA exhibits low cytotoxicity (Fig. S9, ESI[†]). Subsequently, RAW264.7 cells were polarized into M1 and M2 macrophages using LPS and IL-4 stimulation, respectively (Fig. S10, ESI[†]). After incubation of these macrophages with MIL-88B(Fe)@HA over various time points (0, 4, 6, 8, 12, and 24 h), the T_2 contrast effects were evaluated using a 7.0 T MRI system. As shown in Fig. 6e, MIL-88B(Fe)@HA accumulated progressively within both M1 and M2 macrophages, leading to a gradual decrease in T_2 signal intensity. However, M2 macrophages exhibited a less pronounced negative contrast effect compared to M1 macrophages. This difference is attributed to the high GSH levels in M2 cells, which



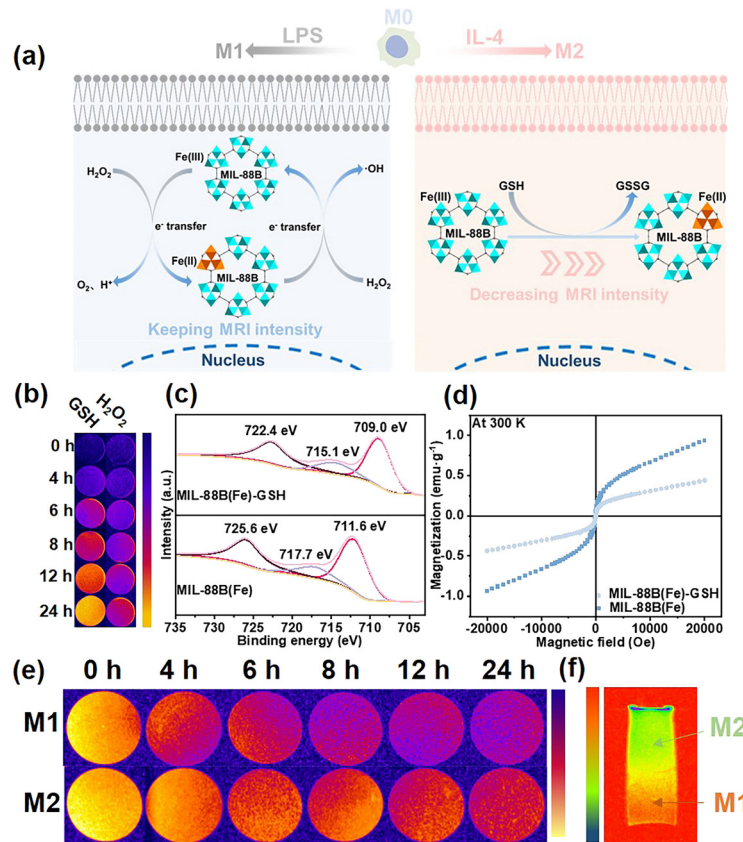


Fig. 6 (a) Schematic illustration of the polarization of M0 macrophages into M1 and M2 macrophages, as well as the chemical reactions occurring during the co-incubation of M1 and M2 macrophages with MIL-88B(Fe)@HA. (b) T_2 -Weighted MR images of GSH mediated reduction of MIL-88B(Fe), alongside the simultaneous oxidation and reduction of MIL-88B(Fe) induced by H_2O_2 in solution at 0 h, 4 h, 6 h, 8 h, 12 h, and 24 h. (c) XPS spectra of Fe 2p levels, and (d) M-H loops at 300 K of MIL-88B(Fe) reduced by GSH. (e) T_2 -Weighted MR images of M1 and M2 macrophages incubated with $50 \mu\text{g mL}^{-1}$ MIL-88B(Fe)@HA for 0 h, 4 h, 6 h, 8 h, 12 h, and 24 h. (f) T_2 -Weighted MR images of the mixed solution of M1 and M2 macrophages incubated with $50 \mu\text{g mL}^{-1}$ MIL-88B(Fe)@HA for 24 h.

reduced Fe(III) to Fe(II), thereby weakening the magnetic response. Moreover, as demonstrated in Fig. 6f, after mixing the solution of M1 and M2 macrophages incubated with MIL-88B(Fe)@HA for 24 hours, a clear differentiation between the two macrophage types was observed under a 7.0 T MRI system. This outcome aligns with the results from the solution-based model experiments, further demonstrating the ability of MIL-88B(Fe) to distinguish between M1 and M2 macrophages based on their distinct biochemical environments. Given that M1 and M2 macrophages coexist in the tumor microenvironment, with M1 macrophages directly attacking tumor cells and contributing to an immune-active environment, the transition from M2 to M1 macrophages is considered crucial for inhibiting tumor progression.^{34–36} The successful validation of this model underscores the potential of Fe-MOFs, such as MIL-88B(Fe), as CAs for monitoring macrophage activity in tumors. Unlike previous studies that rely on cellular uptake to differentiate between M1 and M2 macrophages,³⁷ MIL-88B(Fe) offers a novel and promising approach by exploiting the intrinsic redox-sensitive MRI contrast properties to distinguish macrophage subtypes. This advancement offers a promising approach to cancer diagnosis and therapeutic monitoring.

3. Conclusions

In summary, we systematically investigated the relationship between topology and T_2 relaxivities in four Fe-MOFs based on Fe_3O clusters with similar spherical morphologies and nanoscale sizes. Our results indicate that the acs topology, which has a higher density of Fe_3O clusters, exhibits optimal T_2 relaxivity. In addition, we demonstrated the potential of MIL-88B(Fe) as a promising T_2 CA for monitoring tumor progression, specifically its ability to distinguish between M1 and M2 macrophages. These results provide valuable insights into the design of MOFs with enhanced magnetic properties and offer important guidelines for the development of T_2 CAs in MRI applications.

4. Experimental

4.1. General methods

All materials used in this study were purchased from commercial channels without further purification. Ethylene glycol (EG, 99%), *N,N*-dimethylformamide (DMF, 99.9%), ferric chloride (FeCl_3 , 99%), and ethanol (99.5%) were purchased from



Sinopharm Chemical Reagent Co., Ltd. All other reagents were purchased from Aladdin.

Fourier-transform infrared (FT-IR) spectra were recorded using a Thermo Fisher Nicolet iS10 FT-IR spectrometer. Powder X-ray diffraction (PXRD) data were recorded using a Bruker D8 Advance diffractometer at 40 kV and 40 mA with Cu-K α radiation ($\lambda = 1.5406 \text{ \AA}$). Thermogravimetric (TGA) analyses were performed with a Mettler Toledo TGA/SDTA 851 analyzer under N₂ flow from room temperature to 800 °C with a heating rate of 10 °C min⁻¹. Nitrogen sorption was measured using an ASAP 2020 gas adsorption instrument (Micromeritics) at 77 K. Before gas absorption, the samples were degassed in a vacuum at 100 °C for 24 h. Scanning electron microscopy (SEM) images were taken using a field emission scanning electron microscope (FE-SEM, Ultra55, ZEISS). Transmission electron microscopy (TEM) measurements were conducted using a JEM-2100 microscope (JEOL, Japan) operated at 200 kV. High-resolution TEM (HRTEM) was carried out using an FEI Tecnai F20 microscope. X-ray photoelectron spectroscopy (XPS) spectra were recorded using a PerkinElmer PHI 5000C ESCA system (PerkinElmer, USA). Surface charge was measured using a Zetasizer NanoZS size analyzer (Malvern Instruments, Malvern, UK). Magnetic measurement was carried out using an MPMS (SQUID) VSM magnetometer equipped with a 7.0 T magnet. The magnetization isotherms were collected at 300 K between -2.0 and 2.0 T. Inductively coupled plasma atomic emission spectroscopy (ICP-AES) spectra were recorded using a PerkinElmer Avio 200 optical emission spectrometer. *In vitro* magnetic resonance imaging (MRI) was carried out using a 3.0 T clinical MRI instrument (Discovery MR 750, GE Medical Systems, Milwaukee, WI, USA) and a 7.0 T MR scanner (Novila, Shanghai Chenguang Medical Technology Co., Ltd).

4.2. Preparation of MOFs and Fe₃O cluster

4.2.1. Synthesis of MIL-101(Fe). The synthesis of MIL-101(Fe) was performed according to the procedure reported previously with minor modifications.²⁵ 9 mg of anhydrous ferric chloride (0.055 mmol) was dissolved in 3 mL of ethylene glycol (EG), and 15 mg of terephthalic acid (0.09 mmol) was dissolved in 1 mL of *N,N*-dimethylformamide (DMF). The two solutions were mixed together and stirred at room temperature for 3 hours. The resulting mixture was then transferred to a 20 mL autoclave and reacted at 120 °C for 12 hours, followed by slow cooling down to room temperature. The precipitate was collected by centrifugation, washed sequentially with DMF and ethanol, and dried overnight at 60 °C. The as-made samples were treated with 10 mL of dichloromethane three times and degassed at 150 °C overnight before further analysis. Unless otherwise specified, the post-synthesis procedures for subsequent methods are the same as those described here.

4.2.2. Synthesis of MIL-100(Fe). The synthesis of MIL-100(Fe) was performed according to the procedure reported previously with minor modifications.²⁶ 12 mg of anhydrous ferric chloride (0.074 mmol) was dissolved in 3 mL of EG, and 19 mg of trimesic acid (0.09 mmol) was dissolved in 1 mL of DMF. The two solutions were mixed together and

stirred at room temperature for 3 hours. The resulting mixture was then transferred to a 20 mL autoclave and reacted at 120 °C for 2 hours, followed by slow cooling down to room temperature.

4.2.3. Synthesis of MIL-59(Fe). The synthesis of MIL-59(Fe) was performed according to the procedure reported previously with minor modifications.²⁴ 27 mg of anhydrous ferric chloride (0.166 mmol) was dissolved in 3 mL of EG, and 16 mg of isophthalic acid (0.096 mmol) was dissolved in 1 mL of DMF. The two solutions were mixed together and stirred at room temperature for 3 hours. The resulting mixture was then transferred to a 20 mL autoclave and reacted at 120 °C for 12 hours, followed by slow cooling down to room temperature.

4.2.4. Synthesis of MIL-88B(Fe). The synthesis of MIL-88B(Fe) was performed according to the procedure reported previously with minor modifications.²⁷ 21 mg of anhydrous ferric chloride (0.129 mmol) was dissolved in 3 mL of EG, and 10 mg of terephthalic acid (0.06 mmol) was dissolved in 1 mL of DMF. The two solutions were mixed together and stirred at room temperature for 3 hours. The resulting mixture was then transferred to a 20 mL autoclave and reacted at 120 °C for 2 hours, followed by slow cooling down to room temperature.

4.2.5. Synthesis of [Fe₃O(O₂CPh)₆(H₂O)₃]ClO₄. [Fe₃O(O₂CPh)₆(H₂O)₃]ClO₄ (Fe₃O cluster in short) was prepared as previously reported.³⁸ Solid NaO₂CPh (1.15 g, 8 mmol) was added to a solution of Fe(ClO₄)₃[·]9H₂O (2.06 g, 4 mmol) in MeCN (30 mL). The solution changed from light orange to dark brown-red and was left for slow evaporation. Brown-red crystals formed after a few days, which were filtered off and dried *in vacuo*.

4.2.6. Synthesis of MIL-88B(Fe₂Ga). 14 mg of anhydrous ferric chloride (0.08 mmol) and 7.6 mg of gallium trichloride (0.04 mmol) were dissolved in 3 mL of EG, and 10 mg of terephthalic acid (0.06 mmol) was dissolved in 1 mL of DMF. The two solutions were mixed together and stirred at room temperature for 3 hours. The resulting mixture was then transferred to a 20 mL autoclave and reacted at 120 °C for 2 hours, followed by slow cooling down to room temperature.

4.2.7. Synthesis of MIL-88B(FeGa₂). MIL-88B(FeGa₂) was prepared by the same method as MIL-88B(Fe₂Ga) except replacing anhydrous ferric chloride (14 mg, 0.08 mmol) and gallium trichloride (7.6 mg, 0.04 mmol) with anhydrous ferric chloride (7 mg, 0.04 mmol) and gallium trichloride (15 mg, 0.08 mmol).

4.2.8. Preparation of MIL-88B(Fe)@HA. MIL-88B(Fe) was conjugated with hyaluronic acid (HA) by mixing MIL-88B(Fe) with HA at a weight ratio of 5:1 in an aqueous solution for 24 h.³⁹

4.3. Reaction of MIL-88B(Fe) with glutathione (GSH) and hydrogen peroxide (H₂O₂) in solution

0.2 g L⁻¹ MIL-88B(Fe) was added to the GSH or H₂O₂ solution (6 mmol L⁻¹).⁴⁰ After being ultrasonically dispersed, the solution was taken at 0 h, 4 h, 6 h, 8 h, 12 h, and 24 h for detecting the MRI signal intensity.



4.4. Polarization of M0 macrophages into M1 and M2 macrophages *in vitro*

RAW264.7 cells were seeded in 6-well plates and stimulated with 20 ng mL⁻¹ interleukin 4 (IL-4) and 100 ng mL⁻¹ lipopolysaccharide (LPS) for 24 h to polarize them into M2 and M1 macrophages.

4.5. Cell cytotoxicity

The cytotoxicity of MIL-88B@HA on RAW264.7 cells was evaluated using the Cell Counting Kit-8 (CCK-8) assay. RAW264.7 cells were harvested by trypsinization and seeded in a 96-well cell culture plate at 1×10^4 cells per well and incubated for 24 h at 37 °C under 5% CO₂. Then, the RAW264.7 cells were cocultured with 12.5–200 µg mL⁻¹ MIL-88B(Fe)@HA for 24 h. The CCK-8 solution was then (10 µL per well) added to each well, and incubated at 37 °C for 2 h. Absorbance at 450 nm was measured using a multi-well spectrophotometer (BioTek Instruments, Inc., mit Hauptsitz in Winooski, VT, USA).

4.6. *In vitro* MRI assay

In vitro MRI measurements were performed at 3.0 T and 7.0 T. T_2 testing and T_2 -weighted MR images were performed under the following parameters: TR/TE = 2.5 s/15.69 ms, 128 × 128 matrices, 45 × 45 mm² fields of view, sweep width (SW) = 20 kHz, a slice thickness of 800 µm. Samples were dispersed in xanthan gel (0.2 wt%) at various iron concentrations, while the xanthan gel was used as a control. The specific relaxivity values of r_2 were calculated through the curve fitting of $1/T_2$ (s⁻¹) vs. concentration of Fe (mg mL⁻¹).

4.7. Cellular MRI

50 µg mL⁻¹ MIL-88B(Fe)@HA nanoparticles were incubated with M2 and M1 macrophages for 0 h, 4 h, 6 h, 8 h, 12 h, and 24 h. After that, the cells were washed three times with PBS. Cellular MRI experiments were performed on sample aqueous solution (8×10^5 cells) in 2.5 wt% agarose gel (2 mL). T_2 -Weighted MR images were acquired under the following parameters: TR/TE = 2.5 s/15.69 ms, 128 × 128 matrices, 45 × 45 mm² fields of view, sweep width (SW) = 20 kHz, and a slice thickness of 800 µm. For preparing a mixed solution of M2 and M1 macrophages, first M1 macrophages were dispersed in 1 mL of agarose solution and cooled down to room temperature. Then M2 macrophages dispersed in 1 mL of agarose solution were added into the above solution.

Author contributions

Qiao Wang: methodology and original draft preparation. Yimin Gong and Jianing Li: visualization and investigation. Dan Luo and Xin Zeng: methodology and preparation. Yun Ling and Yaming Zhou: reviewing and editing. Zhenxia Chen: project administration and validation.

Data availability

The data supporting this paper have been included as part of the main article and the ESI.† The original data of this study are available from the corresponding authors upon reasonable request.

Conflicts of interest

There are no conflicts to declare.

Acknowledgements

The authors gratefully acknowledge financial support from the National Natural Science Foundation of China (grant no. 22275037, 82271966, and 21971045), the Shanghai “Science and Technology Innovation Action Plan” Intergovernmental International Science and Technology Cooperation Program (no. 22520713700) and the Science and Technology Commission of Shanghai Municipality (no. 2024ZDSYS02).

Notes and references

- 1 R. Antwi-Baah, Y. Wang, X. Chen and K. Yu, *Adv. Mater. Interfaces*, 2022, **9**, 2101710.
- 2 E. Terreno, D. Delli Castelli, A. Viale and S. Aime, *Chem. Rev.*, 2010, **110**, 3019–3042.
- 3 Z. Zhou, L. Yang, J. Gao and X. Chen, *Adv. Mater.*, 2019, **31**, 1804567.
- 4 E. J. Werner, A. Datta, C. J. Jocher and K. N. Raymond, *Angew. Chem., Int. Ed.*, 2008, **47**, 8568–8580.
- 5 P. Caravan, J. J. Ellison, T. J. McMurry and R. B. Lauffer, *Chem. Rev.*, 1999, **99**, 2293–2352.
- 6 N. Kuznik and M. Wyskocka, *Eur. J. Inorg. Chem.*, 2016, 445–458.
- 7 P. Caravan, *Chem. Soc. Rev.*, 2006, **35**, 512–523.
- 8 C.-T. Yang, P. Padmanabhan and B. Z. Gulyas, *RSC Adv.*, 2016, **6**, 60945–60966.
- 9 G. J. Soufi, A. Hekmatnia, S. Iravani and R. S. Varma, *ACS Appl. Nano Mater.*, 2022, **5**, 10151–10166.
- 10 M. Jeon, M. V. Halbert, Z. R. Stephen and M. Zhang, *Adv. Mater.*, 2021, **33**, 1906539.
- 11 Y. W. Jun, Y. M. Huh, J. S. Choi, J. H. Lee, H. T. Song, S. Kim, S. Yoon, K. S. Kim, J. S. Shin, J. S. Suh and J. Cheon, *J. Am. Chem. Soc.*, 2005, **127**, 5732–5733.
- 12 Z. Zhao, Z. Zhou, J. Bao, Z. Wang, J. Hu, X. Chi, K. Ni, R. Wang, X. Chen, Z. Chen and J. Gao, *Nat. Commun.*, 2013, **4**, 2266.
- 13 O. M. Yaghi, M. O’Keeffe, N. W. Ockwig, H. K. Chae, M. Eddaoudi and J. Kim, *Nature*, 2003, **423**, 705–714.
- 14 L. Li, X. Cao and R. Huang, *Chin. J. Chem.*, 2016, **34**, 143–156.
- 15 P. Horcajada, T. Chalati, C. Serre, B. Gillet, C. Sebrie, T. Baati, J. F. Eubank, D. Heurtaux, P. Clayette, C. Kreuz, J.-S. Chang, Y. K. Hwang, V. Marsaud, P.-N. Bories,

L. Cynober, S. Gil, G. Ferey, P. Couvreur and R. Gref, *Nat. Mater.*, 2010, **9**, 172–178.

16 T. Qiu, T. Wu, M. Lu, Y. Xie, M. Zhang, D. Luo, Z. Chen, B. Yin, Y. Zhou and Y. Ling, *Small*, 2023, **19**, 2303063.

17 P. Hirschle, C. Hirschle, K. Boell, M. Doeblinger, M. Hoehn, J. M. Tuffnell, C. W. Ashling, D. A. Keen, T. D. Bennett, J. O. Raedler, E. Wagner, M. Peller, U. Laechelt and S. Wuttke, *Chem. Mater.*, 2020, **32**, 2253–2263.

18 S. M. McLeod, L. Robison, G. Parigi, A. Olszewski, R. J. Drout, X. Gong, T. Islamoglu, C. Luchinat, O. K. Farha and T. J. Meade, *ACS Appl. Mater. Interfaces*, 2020, **12**, 41157–41166.

19 S. Dehghani, N. R. Alam, S. Shahriarian, T. Mortezaeezadeh, S. Haghgo, A. Golmohamadpour, B. Majidi and M. Khoobi, *J. Nanopart. Res.*, 2018, **20**, 278.

20 X. Wang, M. Xu, W. Fan and D. Sun, *Chin. J. Chem.*, 2023, **41**, 3772–3791.

21 S. Dawood, S. Shaji, G. Pathiraja, Y. Mo and H. Rathnayake, *Phys. Chem. Chem. Phys.*, 2021, **23**, 21677–21689.

22 D. Li, X. Wang, H.-X. Zhao, Y.-P. Ren, G.-L. Zhuang, L.-S. Long and L.-S. Zheng, *Angew. Chem., Int. Ed.*, 2020, **59**, 14409–14413.

23 L.-L. Lv, Y.-X. Sun, C.-X. Ji, S. Ma, J.-W. Ren, W.-W. Wang, J.-P. Zhao, Z.-Y. Liu, Q. Lin, K. Su, Y. He and F.-C. Liu, *Inorg. Chem. Front.*, 2020, **7**, 186–190.

24 D. Feng, K. Wang, Z. Wei, Y.-P. Chen, C. M. Simon, R. K. Arvapally, R. L. Martin, M. Bosch, T.-F. Liu, S. Fordham, D. Yuan, M. A. Omary, M. Haranczyk, B. Smit and H.-C. Zhou, *Nat. Commun.*, 2015, **6**, 5723.

25 D. Lupu, O. Ardelean, G. Blanita, G. Borodi, M. D. Lazar, A. R. Biris, C. Ioan, M. Mihet, I. Misan and G. Popenciu, *Int. J. Hydrogen Energy*, 2011, **36**, 3586–3592.

26 B. Xu, Z. Chen, B. Han and C. Li, *Catal. Commun.*, 2017, **98**, 112–115.

27 P. Horcajada, F. Salles, S. Wuttke, T. Devic, D. Heurtaux, G. Maurin, A. Vimont, M. Daturi, O. David, E. Magnier, N. Stock, Y. Filinchuk, D. Popov, C. Riekel, G. Ferey and C. Serre, *J. Am. Chem. Soc.*, 2011, **133**, 17839–17847.

28 A. A. Talin, A. Centrone, A. C. Ford, M. E. Foster, V. Stavila, P. Haney, R. A. Kinney, V. Szalai, F. El Gabaly, H. P. Yoon, F. Leonard and M. D. Allendorf, *Science*, 2014, **343**, 66–69.

29 Q. L. Vuong, J.-F. Berret, J. Fresnais, Y. Gossuin and O. Sandre, *Adv. Healthcare Mater.*, 2012, **1**, 502–512.

30 P. Gillis, F. Moiny and R. A. Brooks, *Magn. Reson. Med.*, 2002, **47**, 257–263.

31 S. Tong, S. Hou, Z. Zheng, J. Zhou and G. Bao, *Nano Lett.*, 2010, **10**, 4607–4613.

32 D. Yoo, J.-H. Lee, T.-H. Shin and J. Cheon, *Acc. Chem. Res.*, 2011, **44**, 863–874.

33 H.-Y. Tan, N. Wang, S. Li, M. Hong, X. Wang and Y. Feng, *Oxid. Med. Cell. Longevity*, 2016, **2016**, 2795090.

34 J. Gao, Y. Liang and L. Wang, *Front. Immunol.*, 2022, **13**, 888713.

35 A. J. Boutilier and S. F. Elsawa, *Int. J. Mol. Sci.*, 2021, **22**, 6995.

36 Z. Strizova, I. Benesova, R. Bartolini, R. Novyseidlak, E. Cecrdlova, L. K. Foley and I. Striz, *Clin. Sci.*, 2023, **137**, 1067–1093.

37 W. Khaled, J. Piraquive, B. Leporq, J. H. Wan, S. A. Lambert, N. Mignet, D. Bich-Thuy, S. Lotersztajn, P. Garteiser and B. E. Van Beers, *J. Magn. Reson. Imaging*, 2019, **49**, 1166–1173.

38 A. N. Georgopoulou, Y. Sanakis, V. Psycharis, C. P. Raptopoulou and A. K. Boudalis, *Hyperfine Interact.*, 2010, **198**, 229–241.

39 W. Cai, H. Gao, C. Chu, X. Wang, J. Wang, P. Zhang, G. Lin, W. Li, G. Liu and X. Chen, *ACS Appl. Mater. Interfaces*, 2017, **9**, 2040–2051.

40 X. Han, N. Wang, W. Zhang, X. Liu, Q. Yu, J. Lei, L. Zhou and G. Xiu, *J. Environ. Chem. Eng.*, 2023, **11**, 109144.

